Dual-model wearable photoacoustic microscopy and electroencephalograph: study of neurovascular coupling in anesthetized and freely moving rats

QIAN CHEN,[1] TIAN JIN,[2] WEIZHI QI,[2] AND LEI XI[2,*]

[1] *School of Electronic Science and Engineering, University of Electronic Science and Technology of China, Chengdu, 610054, China*
[2] *Department of Biomedical Engineering, Southern University of Science and Technology, Shenzhen, Guangdong, 518055, China*
*xilei@sustech.edu.cn

Abstract: Observing microscale neurovascular dynamics under different physiological conditions is of great importance to understanding brain functions and disorders. Here, we report a dual-model wearable device and an auxiliary data processing algorithm to derive neurovascular dynamics. The device integrates high-resolution photoacoustic microscopy and electroencephalography (EEG), which allows observing capillary-level hemodynamics and neural activities in anesthesia and freely moving rats. By using the developed algorithm, multiple photoacoustic/EEG parameters extracted and correlated enables investigation of the interplay between neural and vascular activities. We employed this platform to study the neurovascular coupling during different types of seizures in rats under various physiological conditions. We observed cerebral vascular vasodilation/constriction corresponding well to the seizure on/off in rats under regular anesthesia conditions, showing a strong neurovascular coupling coefficient. In rats under weak anesthesia and freely moving conditions, more intense cerebral hemodynamics and neural activities occurred with a weaker neurovascular coupling coefficient. The comprehensively quantitative analyses suggest that anesthesia has a dominant impact on the seizure onset and affect the neurovascular coupling correlation in the current drug-induced localized seizure model. Our study reveals that the designed platform has the potential to support studies on brain functions and disorders in diseased rodent models in various physiological states.

1. Introduction

In recent decades, interpretation of hemodynamics and neural activities has been of great importance in the study of brain functions and disorders. Neurovascular coupling remains the major focus of neuroscience, which aims to investigate the relationships of hemodynamics and neural activities [1,2]. Existing studies show that the dynamics of blood flow and total hemoglobin have a tight relationship with local field potential (LFP) activities [3,4]. Compared to directly exploring the human brain, the use of rodent models for human brain studies is easier and faster. Functional magnetic resonance imaging (fMRI) based on the blood-oxygen-level-dependent (BOLD) method has been extensively used in humans [5–7]. However, to achieve sufficient signal-to-noise ratio (SNR) and spatial resolution for the rodent brain, high magnetic fields, small voxel size, and complicated compensations for inhomogeneities are required. In addition, it is challenging for fMRI to observe capillary-level hemodynamics due to the limited spatiotemporal resolution. Furthermore, due to the bulky size and complicated system design, fMRI can only image anesthetized rodents, preventing studies from investigating rodent brains under different physiological conditions.

Optical imaging modalities have been well developed for studying brain functions with a rich contrast and high spatiotemporal resolution [8–11]. Prior investigations have deeply explored the miniaturization for various optical imaging modalities [8,9]. These miniaturized microscopes have provided a number of unique insights into cellular activities during behaviors, while suffered inherent limitations such as small field of view (FOV) and lack of depth information. Among all the optical imaging modalities, photoacoustic imaging (PAI) takes advantages of rich optical contrast and deep acoustic penetration, which has capability for vascular imaging without external contrast agents [10,11]. PAI is ultrasensitive to hemoglobin in the visible spectra, leading to a high contrast for visualizing vasculatures, and owns a deeper penetration depth owing to a lower acoustic scattering property of biological tissue compared with that of optical photons [12–15]. Existing photoacoustic studies have already demonstrated that intensive/abnormal neural activities in diseased or electro-stimulated models affect local vasculature, such as vasodilation/constriction of blood vessels, and increased blood flow velocity and oxygen metabolism [16,17].

However, most of the studies were carried out using anesthetized rodents due to the bulky size and complicated operations of PAI systems, which makes it challenging to study rodent brains under different physiological conditions or in specific environments [12,18]. To study the neural and vascular dynamics in the awake brain, head-restrained and head-mounted photoacoustic imaging technologies have been applied into various disease models such as seizure and electrostimulation [19–22]. Among these studies, Cao *et al.* reported the use of the head-restrained high-resolution photoacoustic brain imaging system to investigate the differences between anesthetized and awake brains [19]. Although this approach comprehensively and quantitatively characterized the cerebral hemodynamics and metabolism at the microscopic level, body fixation might generate unclear and ineradicable impacts on brain functions. Compared with the head-restrained approach, the wearable device allows for more flexible and reliable brain studies for rodents under different physiological and diseased conditions [20–22]. Previously, we reported a hybrid photoacoustic/EEG sensor for the investigation of a single blood vessel vasodilation/constriction in correspondence to drastic seizure events [20]. However, one-dimensional (1D) imaging restricted the studies to a limited brain region.

Here, we report a wearable device that integrates optical-resolution photoacoustic microscopy (PAM) and EEG for comprehensive and quantitative characterization of cerebral neurovascular dynamics in both anesthetized and freely moving rodents. In addition to longitudinal recording of photoacoustic and associated local field potential (LFP) data, we proposed algorithms to derive hemodynamic and neural parameters and further interpret the interplay between neural activities and hemodynamics of rat brains under different depths and in freely moving rats. We expect that our observations may provide guidance for seizure studies, and we believe that the designed platform is able to support studies on brain functions and disorders in rodents under diverse physiological conditions.

2. Methods

2.1. Animal preparation and surgery

Female Sprague-Dawley female rats weighing 200 to 250 g were used (8-10 weeks, N=13). Throughout the study, animals were kept on a 12:12 hr light cycle with food and water ad libitum. All experimental procedures were approved by the institutional Animal Care and Use Committee of the Southern University of Science and Technology (SUSTech). For photoacoustic imaging, a cranial window was required to enable the optical penetration without scattering. After being anesthetized by 4 Vol% isoflurane with a gas velocity of 0.4 L/min, rats were laid on the heating pad to keep them at a constant temperature, and the heads were fixed on the stereotaxic apparatus with continuous anesthesia during the entire course of surgical procedures. The hair and scalp were removed to expose the skull. We used a marker pen to circle the region of interest (ROI) with a diameter of ~7 mm in the left hemisphere and then thinned the skull in the ROI with a

cranial drill. Once the skull was thin (~50 μm) enough, we carefully used a tweezer to remove the skull and expose the dura for later localized seizure induction, photoacoustic imaging, and LFP recording. After that, the dental cement was subsequently used to cover the surface of the exposed skull except for the imaging area. Inside the window, photoacoustic imaging covers a FOV of ~2×2 mm^2. The localized seizure was established by injecting 4 μL 4-Aminopyridine (1.5 mg/mL) into the left hemisphere cortex near the imaging area. The injection was finished within 30 seconds, which can induce epileptic activities locally for longer than 2 hours. For LFP recording, the positive electrode (injection needle) was positioned ~2 mm close to the imaging area with a ~500 μm inserting depth, the negative electrode was positioned at cerebellum, and the reference electrode was connected to the ground. During the whole procedure, the dura needed to be continually immersed in artificial cerebrospinal fluid to be kept wet.

2.2. Seizure models with animal in different conditions

We divided all rats into 4 groups (Groups A, B, C and D) and established the localized seizure by injecting 4 μL 4-AP (1.5 mg/mL) into the left hemisphere cortex near the imaging area. With the same gas velocity of 0.4 L/min, the concentrations of isoflurane were 3 Vol%, 1.5 Vol%, and 0.5 Vol% for Groups A, B and C, respectively, to establish different anesthesia conditions. No isoflurane was used for the Group D rats, which were awake and freely moving.

2.3. System configuration

Figure 1(a) shows the schematic of the dual-model PAM/EEG system. The 532 nm laser pulses are emitted from a nanosecond pulsed laser (GLPM-10, IPG Photonics) with a duration of ~1.8 nanoseconds (ns) and an experimental repetition rate of 50 kHz. The reflected laser beam is detected by a fast photodiode (PD818-BB-21, Newports Corp.) to record the fluctuations of the laser energy and synchronize the laser scanning and data acquisition. The transmitting laser beam is filtered by an optical spatial filter system consisting of two 10× objectives (O1-O2, RMS10×, Olympus) and a 15-μm pinhole (P15D. Thorlabs Inc.), converged by a 4× objective (O3, RMS4×, Olympus), coupled into the import side of a single mode fiber using a fiber coupler (APFC-5T-FC, Beijing Zolix Intruments Co.). An optical rotary joint (MJP-532-46-FC, Princetel Inc.) and a customized electrical slip ring are integrated to allow for both electrical and optical transmission during the movement of the rat. The detected PA signal amplified *via* a ~60 dB customized amplifier and a bandpass filter (2 MHz to 20 MHz) is collected by a high-speed data acquisition card (ATS 9325, Alazar Inc.). The functional generator is used to drive the MEMS mirror (SWITCH S3.1, Wiotek) to scan the laser beam. The LFP signal is recorded by a physiological recording instrument (RM6240BD, Chengdu instruments) during the entire course of experiments. Figure 1(b) illustrates the detailed structure of the miniaturized probe. The output laser beam from the single mode fiber is collimated by an adjustable collimator (CFC-5X-A, Thorlabs Inc.), reflected by a right-angle prism (MRAP1-4.0, MT Optics) and focused using a Plano-convex lens (LA 1222-A, Thorlabs Inc.) with an aperture value of 0.2. The focused laser beam is reflected and scanned by the MEMS mirror, passes a water cube and reaches the tissue surface.

   In the water cube, an ultrathin cover glass is tilted at a 45° angle to allow for the transmission of light and reflection of acoustic waves. At the right side of the cube, a flat ultrasonic transducer with a center frequency of 10 MHz is used to detect the acoustic waves. At the left side, a fine needle (U40/1 μL) with one tip connected to a commercial micro-syringe (Hamilton701N, 10ul, SYR.) using a transparent tube (ID=0.3 mm, OD=0.8 mm, length~20 mm) is positioned for both 4-AP injection and EEG signal recording. The injection is performed by a microinjection system (ZS-KES-II, China) and finished in 30 s. Benefitting from the miniaturized optical/electro components and ultra-compact design, the imaging probe has a weight of ~10 g, which can be mounted on the rodents head. It has an imaging speed of 5 s with a FOV of ~2×2 mm^2.
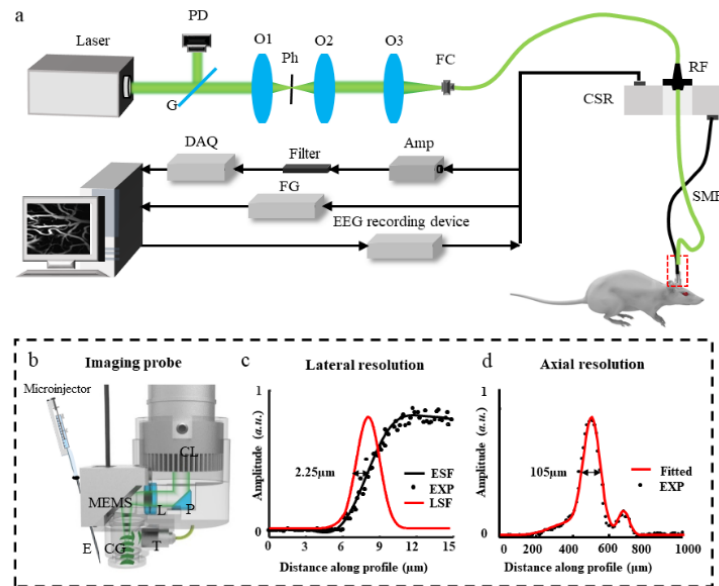
Fig. 1. The schematic depicting the wearable photoacoustic microscopy/EEG probe and evaluation of the imaging performance. (a) The configuration of the system. PD, photodiode; G: ultra-thin transparent glass; O1-O3, objective; Ph, pinhole; FC, fiber coupler; SMF, signal mode fiber; DAQ, data acquisition card; Amp, amplifier; FG, functional generator; RF, optical rotary joint; CSR, conductive slip ring; (b) The enlarged inside view of the wearable probe. CL, zoom collimator; P, right angle prism; L, lens, MEMS, mechanical and electrical system mirror; CG, cover glass; T, transducer; E, electrode. (c) Raw (black spots) data and Gaussian-fitted (black line) edge spread function of the imaged blade. The derived LSF (red) was used to estimate the lateral resolution. (d) Raw (black spots) data and Gaussian-fitted (red) profiles of a typical Hilbert-transformed one-dimensional PA signal. The fitted profile was used to estimate the axial resolution. ESF, edge spread function; LSF, line spread function; EXP, experimental data.

We employed blade experiments to evaluate the spatial resolution of PAM as described in our previous studies [22]. As shown in Figs. 1(c) and 1(d), the systemic lateral and axial resolutions were measured to be 2.25 μm and 105 μm, respectively.

2.4. Hemodynamic and LFP analysis

The amplitude of photoacoustic signal is positively proportional to the concentration of total hemoglobin (C_{HbT}) at 532 nm; thus, we could derive the relative change in C_{HbT} using the fluctuation of photoacoustic amplitude. For each experiment, a series of longitudinal photoacoustic images with a frame size of $m \times n$ pixels were acquired. Figure 2 shows the pretreatment process of all raw images and the extraction of interested parameters. Firstly, to remove the potential movements caused by breathing and injection of 4-AP, we processed all raw images by using a non-rigid image registration method, namely, affine translation. Then, we enhanced the figure contrast of corrected images by using histogram averaging and spatially smoothed all enhanced images by applying a Gaussian filter with a template matrix size of 3×3 pixels. For registered images, we orderly chose each pixel as a node and extracted its photoacoustic projected values at different time spots to form time sequences $P_i(t)$ ($i=1,2,\ldots, m \times n$) which were smoothed for later calculation. At the same time, we removed some external electrical noise of the EEG signal by wavelet transformation and extracted its envelope. All photoacoustic/EEG parameters and

two correlation coefficients were calculated based on the time sequences and the envelope of the de-noised EEG signal. The detailed calculations are explained in the following equations:
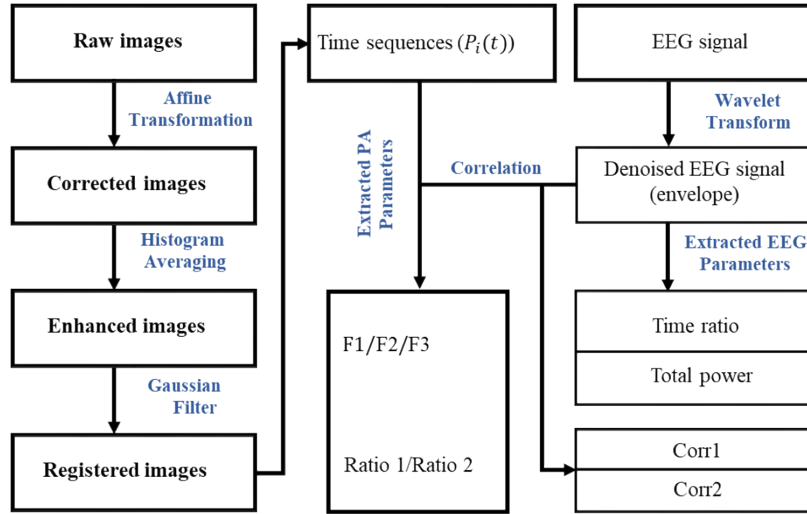

Fig. 2. The schematic of imaging preprocess and extraction of photoacoustic/EEG parameters. F_1, fractional change of C_{HbT} over the entire imaging area; F_2, fractional change of C_{HbT} in interested vascular area; F_3, fractional change of C_{HbT} in the brain tissue; *Ratio 1*, the percentage of pixels with a variance of more than 40% in the entire imaging area; *Ratio 2*, the percentage of pixels with a variance greater than 40% in the vascular contour area.

For a registered image I_0 with a matrix size of $m \times n$. The ith node time sequence $P_i(t)$ ($i = 1, 2, \ldots, m \times n$; $t = 1, 2, 3, \ldots, 60$) was extracted, and its fractional change P_i can be defined as

$$P_i = \frac{P_i(t)_{max} - P_i(0)}{P_i(0)} \tag{1}$$

where $P_i(0)$ is the photoacoustic amplitude of the ith node time sequence $P_i(t)$ at the beginning of the experiment (t=0). Based on fractional change of each node P_i, we defined the fractional change of C_{HbT} over the entire imaging area as F_1:

$$F_1 = \frac{1}{m \times n} \sum_{i}^{m \times n} P_i (i = 1, 2, 3, \ldots, m \times n.) \tag{2}$$

In order to evaluate the hemodynamic response of all blood vessels over the entire imaging area, we calculated the fractional change of C_{HbT} in the vascular area (F_2), by extracting blood vessels in which the fractional change value of brain tissue pixels was set to zero. Thus, F_2 is calculated by

$$F_2 = \frac{1}{N_0} \sum_{i}^{m \times n} P_i (P_i > 0)(i = 1, 2, 3, \ldots, m \times n.) \tag{3}$$

where N_0 is the number of pixels inside the extracted vascular area.

To calculate the fractional change of C_{HbT} in the brain tissue (F_3), we first segmented vascular pixels from the registered image I_0 and obtained a brain tissue image I_1 in which the value in

vascular pixels was set to zero. Thus, F_3 is obtained from

$$F_3 = \frac{1}{N_1} \sum_i^{m \times n} P_i(P_i > 0)(i = 1, 2, 3, \ldots, m \times n.) \tag{4}$$

where N_1 is the number of pixels that are non-zero in the brain tissue.

The repetitive experiments and data analysis help us derive a threshold of 40% for fractional change to distinguish and display the hemodynamic differences among various types of seizures. *Ratio*1 is defined as the percentage of pixels with a variance of more than 40% in the entire imaging area. It is calculated by

$$Ratio1 = \frac{N_2}{m \times n} \tag{5}$$

where N_2 is the pixel number of P_i with a variance greater than 40% in the entire imaging area.

In order to evaluate the fractional change ratio induced by vasodilation/constriction only, we excluded the internal pixels in blood vessels, extracted the contours of blood vessels, and calculated the percentage (*Ratio2*) of pixels with a variance greater than 40% in the vascular contours area. *Ratio2* is defined as the percentage of pixels with a variance greater than 40% in the vascular contour. *Ratio 2* is defined by

$$Ratio2 = \frac{N_3}{N_4} \tag{6}$$

where N_3 is the pixel number of P_i with a variance greater than 40% in the vascular contour, while N_4 is all the pixel numbers of P_i in the vascular contour.

Besides the photoacoustic parameters, we also calculated the electrical parameters based on LFP. The LFP was collected at a sample rate of 800 Hz, and band passed filtered between 0.1 Hz and 400 Hz. The time ratio (time ratio = $\frac{t_{seizure\ on}}{t_{total}}$) and the total power of LFP were calculated and compared among the four groups. In addition, we calculated all correlation coefficients between each node time sequences and the envelope of LFP by using Pearson correlation. *Corr1* represents the maximal correlation coefficients of a single node. In order to evaluate and compare the global correlation over the entire imaging area in different seizure conditions, we excluded the correlation values <0.3 in the brain tissue, and calculated the averages of the rest of the correlation values, which is defined as *Corr2*. We set a threshold of 0.3 due to the maximal correlation value in control case is around 0.3, which is considered as insignificant for evaluating the correlation between hemodynamic responses and neural activities.

2.5. Data analysis

All parameters were calculated using MATLAB 2018. Among these parameters, the Pearson correlation coefficient was used to examine the relationship between hemodynamics and LFP signals. Statistical analysis and graphic display of data in Fig. 5 were performed by Graphpad Prism 6 (San Diego, California). All statistical data are denoted in the format of mean ± standard deviation (SD), unless stated otherwise.

3. Results

3.1. Neurovascular coupling based on a localized seizure model

To verify the capability of the technique for brain imaging and neurovascular coupling, we established a localized seizure model as well as a control case using rats under regular anesthesia conditions, then investigated the relationship of hemodynamics and neuronal actions based on the recorded sequential PA and LFP data. Figure 3(a) shows a series of photoacoustic images acquired throughout the entire course of the seizure and control experiments. Each map has a

matrix size of 500×500 pixels. Figure 3(b) shows the LFPs and the sequential PA amplitudes of single selected blood vessels marked by the red lines in Fig. 3(a) for both the seizure and control cases. In the seizure case, the similar variance tendency represents a good vascular response to the LFP before and after the seizure occurrence, revealing a possible tight relationship between hemodynamics and neuronal activities. In contrast, the control case shows consistent flat curves of the EEG signal and PA amplitude before and after injection of phosphate buffered saline. To further verify the interplay of neurovascular dynamics, PA time sequences of different nodes and the envelope of LFP were extracted to derive the interested parameters and then evaluate neurovascular coupling, as shown in Figs. 3(c) to 3(i). Figure 3(c) shows that PA time sequences of all nodes on the PA MAP image were orderly derived, and ten-minute data, highlighted by the grey rectangle area, correlated with the corresponding LFP envelope. Figure 3(d) is the correlation map, indicating that various blood vessels have similar or discrepant relationships with the corresponding LFP. Figure 3(e) shows the max fractional change map calculated by extracting the max fractional change of the time sequence of each node in Fig. 3(c), in which the large value of the edges of blood vessels is caused by the dilation and contraction of blood vessels. Based on the max fractional change map, we also obtained the max fractional change map (>40%) and the edge contour structure map of vasculature, as shown in Fig. 3(f). Figures 3(g) - (i) are the results of the control case using the same processing procedure. In the control case, the correlation values and hemodynamic fractional change were smaller than those of the epileptic case. There were no segmented nodes with a fractional change > 40% in the control case, as shown in Fig. 3(i). Visualization 1 and Visualization 2 show the real-time neurovascular dynamics of the seizure case and the control case, respectively. These results demonstrate the feasibility of the proposed technique for studying neurovascular coupling.

3.2. Hemodynamic responses to epileptic activities under various physiological conditions

In rats under different anesthesia and awake conditions, we generated four types of localized seizures and monitored their cerebral hemodynamic responses to epileptic activities. In detail, type A, type B, and type C represented different depths of anesthesia: concentrations of isoflurane were 3 Vol%, 1.5 Vol%, and 0.5 Vol%, respectively, with the same gas velocity of 0.4 L/min each. Type D means that the rats were awake and freely moving. The localized seizure model was induced by the injection of the same dose of 4-AP to the exposed area of all the rats. Longitudinal photoacoustic imaging and LFP recording were carried out for 40 minutes. Figures 4(a), 4(c), 4(e) and 4(g) show the photoacoustic MAP images and LFPs of four representative rats in the four different seizure cases. Vasculature in red boxes is enlarged and placed to show the hemodynamic responses at different time points (I, before injection; II, before seizure onset; III, seizure on; IV, seizure off). The hemodynamics response demonstrates that regular vascular diastole and persistent expansion correspond to intermittent and continuous epileptic activities. Figures 4(b), 4(d), 4(f) and 4(h) show longitudinal variances of relative C_{HbT} in the selected areas (L_C_{HbT}), the entire area (T_C_{HbT}) and brain tissue (ST_C_{HbT}), the PA amplitude (V_PA) and diameter (V_D) of a selected blood vessel. These curves correspond to the LFPs with a 20-minute time window, highlighted by the grey dash box in Figs. 4(a), 4(c), 4(e), and 4(g). By using the proposed neurovascular coupling algorithm, all correlation maps, hemodynamic fractional change maps and vascular contours maps of the four experimental seizure cases were calculated and compared, as shown in supplementary Fig. 1. All photoacoustic/EEG parameters and correlation coefficients were also quantified, as shown in supplementary Table 1. The real-time neurovascular dynamics of the four seizure cases can be seen in Visualization 3, Visualization 4, Visualization 5, Visualization 6.
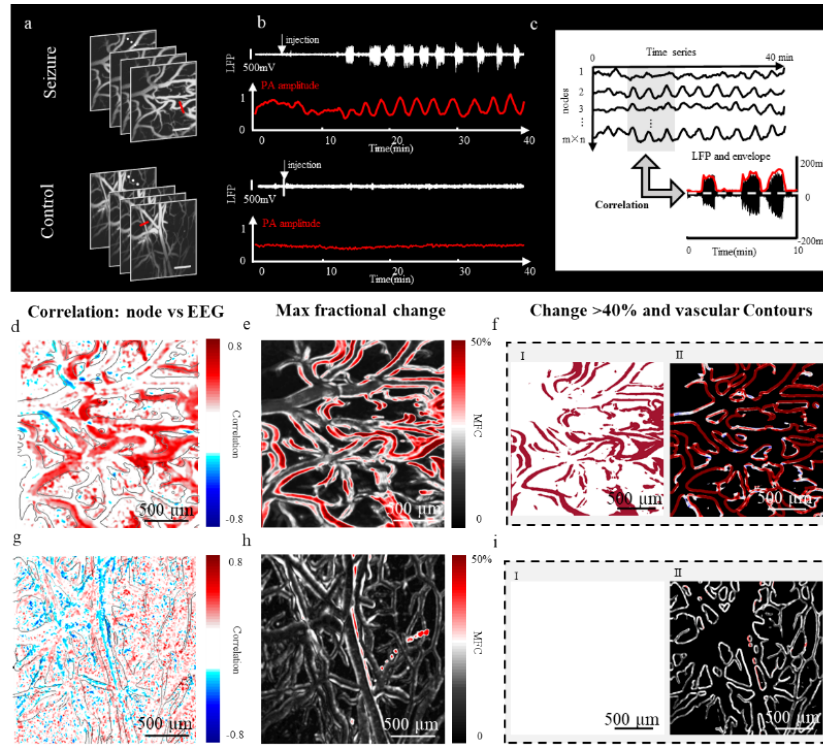
Fig. 3. Validation of the neurovascular coupling method based on the localized focal seizure and control cases. (a) Time sequences of typical PA MAPs of seizure and control cases, respectively. Scale bar, 500 μm. (b) Time sequences of the recording EEG signals, the responsive vascular hemodynamics of selected single vessels marked by red lines in Fig. 3(a)). In the seizure case, the LFP data shows intermittent seizure, while the vascular hemodynamic change corresponds well before and after each seizure onset. In the control case, both the EEG signal and the PA amplitude of a single blood vessel remained flat. (c) (Taking the seizure case as an example) The correlation between the time sequences of the nodes in PA MAPs and the envelopes. A typical 10-minute PA data (marked by grey box) correlated to the corresponding LFP signal for calculating the correlation coefficients of each node. (d) and (g) The correlation maps calculated using variance sequences of nodes and the envelope of the corresponding EEG signal, in the seizure case (d) and the control case (g). (e) The fractional change maps derived from variance sequences of nodes, in seizure case (e) and control case (h), respectively. MCF, max fractional change of photoacoustic amplitude. (f) and (i) The segmented nodes with fractional change > 40% and edge contour of vasculature extracted from the fractional change map in the seizure case (f) and the control case (i).
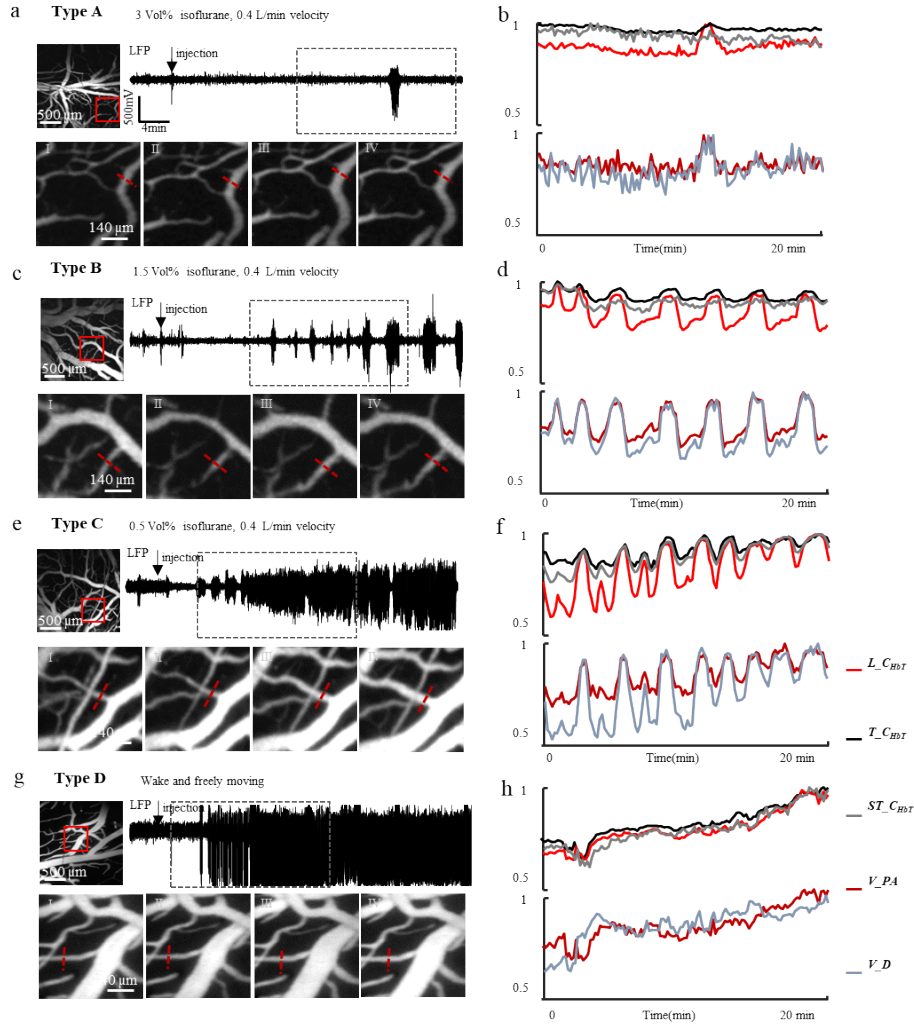
Fig. 4. The hemodynamic responses to epileptic seizure in rats under different anesthesia depths and in freely moving condition. (a), (c), (e) and (g) show the photoacoustic MAP images and LFPs of four rats under various depths of anesthesia and in freely moving condition (3 Vol% isoflurane, 0.4 L/min velocity; 1.5 Vol% isoflurane, 0.4 L/min velocity; 0.5 Vol% isoflurane, 0.4 L/min velocity; awake and freely moving), respectively. Figures I, II, III, and IV are the enlarged views of vasculature marked by red boxes, representing the hemodynamic responses at different time points, demonstrating the phenomenon of vascular vasodilation and constriction. (b), (d), (f) and (h) display the time sequences of L_C_{HbT}, T_C_{HbT}, ST_C_{HbT}, V_PA, and V_D within 20 minutes, corresponding to the LFPs marked with dashed rectangles in (a), (c), (e), and (g), respectively. L_C_{HbT}, local hemoglobin; T_C_{HbT}, total hemoglobin; ST_C_{HbT}, brain tissue hemoglobin concentration; V_PA, photoacoustic amplitude of a single vessel; V_D, diameter of a single vessel.
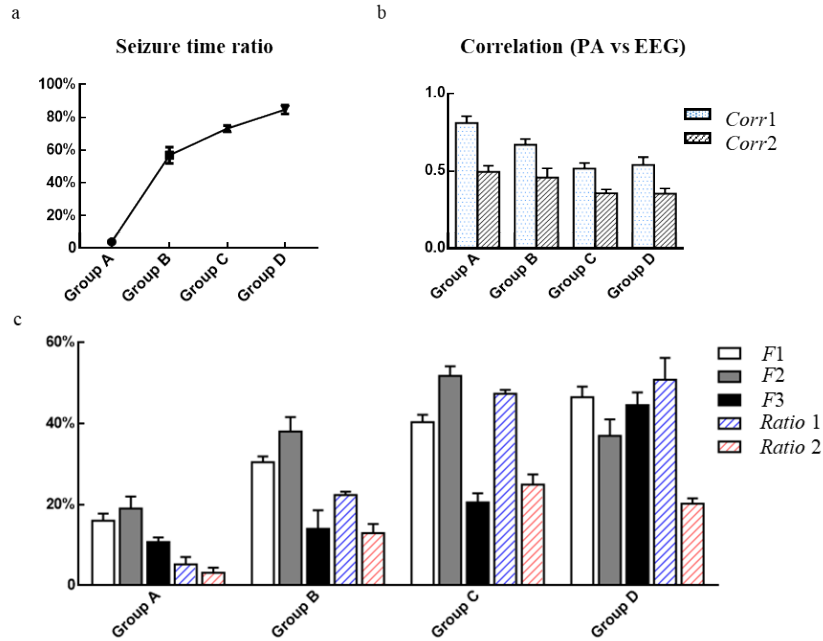
Fig. 5. The statistical comparison of hemodynamic responses to epileptic seizures in four groups of rats under different anesthesia depths and in freely moving condition. (a) The seizure time ratio of the data for the four groups. (b) The correlation coefficients between photoacoustic signal and LFP. *Corr1*, correlation coefficient in a single node position. *Corr2*, the mean correlated value of entire imaging area. (c) Comparing statistics of photoacoustic/EEG parameters between the four groups, including average fractional change of hemoglobin throughout the entire imaging area (F_1), vascular area (F_2), brain tissue (F_3), and two percentages of changed pixels (*Ratio*1 and *Ratio*2). *Ratio*1, the percentage of pixels with a change of more than 40% throughout the entire imaging area; *Ratio*2, the percentage of pixels with a change of more than 40% in the vascular contours area. Mean ± SD.

3.3. Statistics and comparison of hemodynamic responses to four types of seizures

To characterize the cerebral hemodynamic responses to seizures at the statistical level, we repeated four types of seizure experiments with 3 rats in each group. As shown in Fig. 5(a), the seizure time ratios of the four groups were 3.9% (±0.6% n=3), 56.8% (±5% n=3), 73.1% (±1.8% n=3), and 84.7% (±2.7% n=3), showing obvious differences between the different types of seizures. Figure 5(b) shows the statistical correlation between cerebral hemodynamics and neuronal activities, including the correlation coefficient in a single node position (*Corr1*) and the average correlated value of the total area (*Corr2*). The results show that the more drastically and continuously a seizure occurred, the less correlation of hemodynamic/neuronal activities were. To determine the cerebral hemodynamic changes in the different seizure cases, we repeated each type of seizure case three times and obtained a statistical analysis, as shown in Fig. 5(c). These statistical photoacoustic/EEG parameters include the average fractional changes of C_{HbT} for the entire, the selected vascular, and the brain tissue areas (F_1, F_2, F_3) and two percentages of changed pixels (*Ratio1*, *Ratio2*). In detail, the calculated average fractional changes of C_{HbT} for the entire imaging area were 16.0% (±3%, n=3), 30.4% (±2.5%, n=3), 40.3% (±3.2%, n=3), and 46.4% (±4.6%, n=3) for Groups A, B, C and D, respectively. These data demonstrate that the more severely a seizure occurred, the higher the fractional change of vascular hemodynamics were, which is in accordance with the phenomenon in Figs. 4(a), 4(c), 4(e) and 4(g). For the

selected vascular and brain tissue areas, fractional changes in the four groups were 19.0% (±5.1%, n=3), 38.0% (±6.2%, n=3), 51.7% (±4.1%, n=3), 37.0%(±7.0%, n=3) and 10.7% (±2.1%, n=3), 14.0% (±7.9%, n=3), 20.5% (±3.9%, n=3), 44.5%(±5.5%, n=3), respectively. These data represent that the changes in cerebral hemodynamics of both the entire and the brain tissue areas have similar tendencies. The parameters of *Ratio1* and *Ratio2* were also calculated and compared among the four groups. For example, the values of *Ratio 1* were 5.2% (±3.1%, n=3), 22.3% (±1.4%, n=3), 47.3% (±1.7%, n=3), and 50.8% (±9.4%, n=3), showing an increase in changeable area corresponding to a more severe seizure. The values of *Ratio 2* in the four groups were 3.1% (±2.2%, n=3), 12.9% (±3.9%, n=3), 24.9% (±4.4%, n=3), and 20.2% (±2.3%, n=3), also showing an increase in changeable vascular area in the three anesthetic groups but a slight decline in the freely moving group. These data show that, from a weak seizure under deep anesthetic to an intense seizure under light or freely moving conditions, the calculated photoacoustic/EEG parameters have increasing trends, demonstrating that more hemodynamic fractional changes corresponded to more drastic seizures.

4.   Discussion

This work represents a major advancement in the study of brain functions and diseases using a rodent model. In detail, we report a dual model wearable neurovascular imaging device, promoting a neurovascular coupling method for investigating the interplay between cerebral hemodynamics and neural activities. Firstly, we successfully developed a miniaturized photoacoustic/EEG microscope, providing a platform for neurovascular observation in anesthetized and freely moving rodents. The conventional PAMs usually use bulky motor stages for two dimensional scanning, making it difficult to achieve small, light, and fast imaging devices [12,19,23]. Even though the existing portable or handheld devices using galvanometer scanners or electromagnetic MEMS scanners have greatly reduced the systematic size and weight, they are still too bulky and heavy (hundreds of grams to a few kilograms), which is unsuitable for the investigation of neurovascular coupling using awake and freely moving rodents [24–27]. Our previous work has demonstrated the potential of an electrothermal MEMS scanner for system miniaturization [18,22,26]. The wearable probe in this study employs a miniaturized electrothermal MEMS scanner and optical/electro components to achieve a lighter weight of ~10 g and a volume size smaller than a coin. The proposed wearable device has a higher resolution of 2.25 μm better than the existing benchtop and hand-held PAMs, enables the brain imaging with a FOV of 2 mm×2 mm and an imaging speed of 5 seconds, which is good enough for measuring the hemodynamic response. Combining with EEG technology, it allows neurovascular observation under diverse physiological conditions.

We promoted a neurovascular coupling method based on the time sequences of photoacoustic and LFP signals. By establishing the localized focal seizure model in rats, we verified the feasibility of analyzing neurovascular dynamics and their interplay between each other. The existing studies have shown that a cluster of drastic neuronal activities will cause cerebral vascular vasodilation/constriction and a rise in blood flow velocity and concentration of total hemoglobin, demonstrating the close interplay of neurovascular dynamics [20,28,29]. In our studies, we observed a phenomenon consistent with the previous reports, as shown in Fig. 3(b) and Visualization 2. Specifically, the longitudinal variances of C_{HbT} in interested blood vessels corresponded well to the EEG signal, showing the correlation properties between hemodynamics and neural activities. Furthermore, by preprocessing a series of longitudinal raw photoacoustic images, extracting all node-based time sequences, and analyzing the LFP signal, we obtained the photoacoustic fractional change and the correlation maps. As shown in Figs. 3(d) to 3(f), the correlation map directly shows the close interplay of neurovascular dynamics, while the fractional change maps also accurately quantify changes of various blood vessels. Meanwhile, we used the neurovascular coupling method to study the control case and obtained a weaker

correlation of neurovascular activities and smaller hemodynamic fractional changes compared with the seizure case, as shown in Figs. 3(g) to 3(i). By analyzing and comparing neurovascular dynamics and their interplay in the seizure and control cases, we demonstrated the feasibility of a neurovascular coupling method for investigating brain functions.

In clinical situations, most acute neurovascular diseases occur suddenly. The physiological conditions affect the brain functional activities of the patients. Therefore, it is important to investigate brain functions under different physiological conditions [30,31]. The fundamental researches based on animal models always provide support for clinical studies, and rodents are the most commonly used animals for structural/functional brain studies. Thus, investigation of the hemodynamics and neural activities using rodents under different physiological conditions is of great importance to understanding the diversity of brain activities and the underlying neurovascular coupling [32,33]. Based on the dual-model wearable device and the neurovascular coupling method, we have comprehensively investigated the cerebral hemodynamics and the neural activities in different types of seizure models. In detail, localized seizures were induced in rats under different depths of anesthesia as well as in awake and freely moving rats, and longitudinal neurovascular dynamics monitoring was carried out. The depth of anesthesia was controlled by adjustable concentrations of isoflurane, while the intensity of seizure occurrence was evaluated and compared by calculated values of time ratio and total power of LFPs (Supplementary table l). From the imaging results and associated analysis, we have several conclusions: **1)** in rats under deep and moderate anesthesia (type A and type B seizures in Figs. 4(a-d)), the cerebral vascular vasodilation/constriction corresponded well to the seizure on/off, revealing the close interplay of neurovascular actions. Supplementary Figs. 1(a) and (d) show the correlation maps, and Table 1 demonstrates the high correlation values of neurovascular coupling. **2)** Compared with the regular anesthesia cases, more severe seizures occurred in the rats under weak anesthesia (type C seizure in Fig. 4(e-f)). This caused a higher fractional change in vascular hemodynamics with a weaker correlation to neuronal activities. It is possible that blood vessels gradually lost functions due to a large number of vasodilation, which would also cause the delayed hemodynamic responses and the weak correlation of neurovascular (noun) [34]. **3)** In the freely moving cases (type D in Fig. 4), the occurrence of seizure was the most dramatic one, with the most intense hemodynamics response and the weakest coupling of hemodynamics and neuronal activities. As shown in Figs. 4(g) and 4(h), the blood vessels in the cortex have persistently expanded, and the PA amplitude continuously increased due to an immediate seizure after the injection. Supplementary Table 1 shows that type D had the weakest correlation value among all types. One possible reason is that the excessive vasodilation of blood vessels may damage the pericytes on vascular walls and thus lead to delayed hemodynamic responses and a weak correlation [33,35]. In addition, complex brain functional activities may also have influence on the transmission of epileptic signals, thus affecting the interplay between hemodynamics and neuronal activities when the animal is awake and freely moving [36,37]. To verify our observations, we repeated the four types of seizure experiments with 3 rats in each group, then quantified and compared all photoacoustic/EEG parameters at the statistical level, as shown in Fig. 5. Figure 5(a) shows that the seizure time ratio is a good indicator of the intensity of seizure occurrence. The statistical correlation values in Fig. 5(b) (*Corr1* and *Corr2*) also reveal a decreasing trend with the occurrence of more severe seizures. Similarly, the hemodynamic responses obeyed the rule that higher fractional changes correspond to a more intense seizure, as shown in Fig. 5(c). It is worth noting that the vascular change in freely moving cases was smaller than that in the weak anesthesia cases, yet had lager changes in brain tissue (F_2 and F_3 in Fig. 5(c)). Thus, the freely moving cases still had the largest hemodynamic fractional change over the entire imaging area (F_1 in Fig. 5(c)). This phenomenon is illustrated in supplementary Figs. 1(h) and (k).

This study demonstrates the feasibility of neurovascular imaging with rodents in various physiological conditions, providing the platform for awake and freely moving animal studies (Visualization 7). Additionally, the coupling of neuronal and vascular dynamics represents a unique aspect for understanding functional brain activities in clinical epilepsy researches. In the future, faster laser sources and more sensitive photoacoustic detectors can be employed to enhance the spatiotemporal resolution for faster imaging of neuron/vascular structures. Multi-spectral illumination can also be carried out to obtain more functional parameters and realize more detailed functional connections. Moreover, PAM can be combined with other imaging modalities for integrated brain studies, such as laser speckle imaging for deriving blood flow, fluorescence calcium imaging for directly observing neuronal activities, and the cortical array electrode-based electroencephalography for source localization [38–40]. For chronic neurovascular diseases such as spontaneous epilepsy, Alzheimer's disease (AD), Parkinson's disease (PD), chronic cranial windows (CCW) is desirable for long-term imaging [41–44].

5. Conclusion

In this study, we have developed a miniaturized photoacoustic/EEG microscopic device and applied it to investigate the neurovascular coupling in different types of focal seizures. This imaging device provides high spatiotemporal observation of local cerebral vascular network and neuronal activities in rats under various anesthesia states and in awake conditions. Based on the focal epilepsy rat models, we established a neurovascular coupling method by extracting and analyzing the time sequences of recorded photoacoustic and LFP signals. Some photoacoustic/neural parameters were calculated and quantified to determine the interplay between brain hemodynamics and neuronal activities. Comparing these parameters helps us understand the influence of drastic neural activities on hemodynamics and the differences between various focal seizures under different physiological conditions. Our work provides potential for fundamental or therapeutic studies of seizures. Similarly, some neurovascular diseases, behavioral disorders and cognitive disorders can be investigated with our photoacoustic protocol.

Disclosures. The authors declare no conflicts of interest.

Data availability. Data underlying the results presented in this paper are not publicly available at this time but may be obtained from the authors upon reasonable request.

Supplemental document. See Supplement 1 for supporting content.

References

1. J.L. Fan, J.A. Rivera, W. Sun, J. Peterson, H. Haeberle, S. Rubin, and N. Ji, "High-speed volumetric two-photon fluorescence imaging of neurovascular dynamics," Nat. Commun. **11**(1), 6020 (2020).
2. J.H. Shi, T.T.W. Terence, Y. He, L. Li, R.Y. Zhang, C.S. Yun, J. Hwang, K. Maslov, and L.V. Wang, "High-resolution, high-contrast mid-infrared imaging of fresh biological samples with ultraviolet-localized photoacoustic microscopy," Nat. Photonics **13**(9), 609–615 (2019).
3. S. Harris, H.T. Ma, M.R. Zhao, L. Boorman, Y. Zheng, A. Kennerley, M. Bruyns-Haylett, P.G. Overton, J. Berwick, and T.H. Schwartz, "Coupling between gamma-band power and cerebral blood volume during recurrent acute neocortical seizures," NeuroImage **97**, 62–70 (2014).
4. J.S. Farrell, Q. Greba, T.P. Snutch, J.G. Howland, and G.C. Teskey, "Fast oxygen dynamics as a potential biomarker for epilepsy," Sci. Rep. **8**(1), 17935 (2018).
5. I.N. Christie, J.A. Wells, S. Kasparov, A.V. Gourine, and M.F. Lythgoe, "Volumetric spatial correlations of neurovascular coupling studied using single pulse opto-fMRI," Sci. Rep. **7**(1), 41583 (2017).

6. X.M. Chen, F. Sobczak, Y. Chen, Y.Y. Jiang, C.Q. Qian, Z.N. Lu, C. Ayata, N.K. Logothetis, and X. Yu, "Mapping optogenetically-driven single-vessel fMRI with concurrent neuronal calcium recordings in the rat hippocampus," Nat. Commun. **10**(1), 5239 (2019).

7. H.J. Shim, W.B. Jung, F. Schlegel, J. Lee, S. Kim, J. Lee, and S.G. Kim, "Mouse fMRI under ketamine and xylazine anesthesia: robust contralateral somatosensory cortex activation in response to forepaw stimulation," NeuroImage **177**, 30–44 (2018).

8. W.J. Zong, R.L. Wu, S.Y. Chen, J.J. Wu, H.B. Wang, Z. Zhao, G.Q. Chen, R. Tu, D.L. Wu, Y.H. Hu, Y.Y. Xu, Y. Wang, Z.L. Duan, H.T. Wu, Y.F. Zhang, J. Zhang, A. Wang, L.Y. Chen, and H.P. Cheng, "Miniature two-photon microscopy for enlarged field-of-view, multi-plane and long-term brain imaging," Nat. Methods **18**(1), 46–49 (2021).

9. M.L. Rynes, D.A. Surinach, S. Linn, M. Laroque, V. Rajendran, J. Dominguez, O. Hadjistamoulou, Z.S. Navabi, L. Ghanbari, G.W. Johnson, M. Nazari, M.H. Mohajerani, and S.B. Kodandaramaiah, "Miniaturized head-mounted microscope for whole-cortex mesoscale imaging in freely behaving mice," Nat. Methods **18**(4), 417–425 (2021).

10. B. Guo, J.Q. Chen, N.B. Chen, E. Middha, S.D. Xu, Y.T. Pan, M. Wu, K. Li, C.B. Liu, and B. Liu, "High-resolution 3D NIR-II photoacoustic imaging of cerebral and tumor vasculatures using conjugated polymer nanoparticles as contrast agent," Adv. Mater. **31**(25), 1808355 (2019).

11. C.B. Liu, J.L. Liao, L.C. Chen, J.H. Chen, R.B. Ding, X.J. Gong, C.M. Cui, Z.Q. Pang, W. Zeng, and L. Song, "The integrated high-resolution reflection-mode photoacoustic and fluorescence confocal microscopy," Photoacoustic **14**, 12–18 (2019).

12. J.J. Yao, L.D. Wang, J.M. Yang, K.I. Maslov, T.T.W. Wong, L. Li, C.H. Huang, J. Zou, and L.V. Wang, "High-speed label-free functional photoacoustic microscopy of mouse brain in action," Nat. Methods **12**(5), 407–410 (2015).

13. B. Ning, S.D. Sun, R. Cao, R.M. Chen, K.K. Shung, J.A. Hossack, J.M. Lee, Q.F. Zhou, and S. Hu, "Ultrasound-aided multi-parametric photoacoustic microscopy of the mouse brain," Sci. Rep. **5**(1), 18775 (2016).

14. Q. Chen, W. Qin, W.Z. Qi, and L. Xi, "Progress of clinical translation of handheld and semi-handheld photoacoustic imaging," Photoacoustics **22**, 100264 (2021).

15. J.J. Yao, A.A. Kaberniuk, L. Li, D.M. Shcherbakova, R.Y. Zhang, L.D. Wang, G. Li, V.V. Verkhusha, and L.V. Wang, "Multiscale photoacoustic tomography using reversibly switchable bacterial phytochrome as a near-infrared photochromic probe," Nat. Methods **13**(1), 67–73 (2016).

16. L.D. Liao, M.L. Lic, H.Y. Lai, Y.Y.I. Shi, Y.C. Lo, S.N. Tsang, P.C.P. Chao, C.T. Lin, F.S. Jaw, and Y.Y. Chen, "Imaging brain hemodynamic changes during rat forepaw electrical stimulation using functional photoacoustic microscopy," NeuroImage **52**(2), 562–570 (2010).

17. B. Rao, R.Y. Zhang, L. Li, J.Y. Shao, and L.V. Wang, "Photoacoustic imaging of voltage responses beyond the optical diffusion limit," Sci. Rep. **7**(1), 2560 (2017).

18. H. Guo, Q. Chen, W.Z. Qi, X.X. Chen, and L. Xi, "In vivo study of rat cortical hemodynamics using a stereotaxic-apparatus-compatible photoacoustic microscope," J. Biophotonics **11**(9), e201800067 (2018).

19. R. Cao, J. Li, B. Ning, N.D. Sun, T.X. Wang, Z.Y. Zuo, and S. Hu, "Functional and oxygen-metabolic photoacoustic microscopy of the awake mouse brain," NeuroImage **150**, 77–87 (2017).

20. L. Xi, T. Jin, J.L. Zhou, P. Carney, and H.B. Jiang, "Hybrid photoacoustic and electrophysiological recording of neurovascular communications in freely-moving rats," NeuroImage **161**, 232–240 (2017).

21. J.B. Tang, J.E. Coleman, X.J. Dai, and H.B. Jiang, "Wearable 3-D photoacoustic tomography for functional brain imaging in behaving rats," Sci. Rep. **6**(1), 25470 (2016).

22. Q. Chen, H.K. Xie, and L. Xi, "Wearable optical resolution photoacoustic microscopy," J. Biophotonics **12**(8), e201900066 (2019).

23. H.C.A. Lin, A. Chekkoury, M. Omar, T. Schmitt-Manderbach, B. Koberstein-Schwarz, T. Mappes, H. Lopez-Schier, D. Razansky, and V. Ntziachristos, "Selective plane illumination optical and optoacoustic microscopy for postembryonic imaging," Laser Photonics Rev. **9**(5), L29–L34 (2015).

24. T. Jin, H. Guo, H.B. Jiang, B.W. Ke, and L. Xi, "Portable optical resolution photoacoustic microscopy (pORPAM) for human oral imaging," Opt. Lett. **42**(21), 4434–4437 (2017).

25. K. Park, J.Y. Kim, C. Lee, S. Jeon, G. Lim, and C.H. Kim, "Handheld photoacoustic microscopy probe," Sci. Rep. **7**(1), 13359 (2017).

26. Q. Chen, H. Guo, T. Jin, W.Z. Qi, H.K. Xie, and L. Xi, "Ultracompact high-resolution photoacoustic microscopy," Opt. Lett. **43**(7), 1615–1618 (2018).

27. C. Lu, K.D. Xiong, Y.Z. Ma, W.Y. Zhang, Z.W Cheng, and S.H. Yang, "Electrothermal -MEMS-induced nonlinear distortion correction in photoacoustic laparoscopy," Opt. Express **28**(10), 15300–15313 (2020).

28. O. Prager, L. Kamintsky, L.A.H. Henderson, K. Schoknecht, V. Wuntke, I. Papageorgiou, J. Swolinsky, V. Muoio, G.B. Klein, U. Vazana, U. Heinemann, A. Friedman, and R. Kovács, "Seizure-induced microvascular injury is associated with impaired neurovascular coupling and blood-brain barrier dysfunction," Epilepsia **60**(2), 322–336 (2019).

29. T. Matsui, T. Murakami, and K. Ohki, "Neuronal origin of the temporal dynamics of spontaneous BOLD activity correlation," Cerebral Cortex **29**(4), 1496–1508 (2019).

30. I. Guadilla, B. Lizarbe, L. Barrios, S. Cerdán, and P.L. Larrubia, "Integrative analysis of physiological responses to high fat feeding with diffusion tensor images and neurochemical profiles of the mouse brain," Int. J. Obes. **45**(6), 1203–1214 (2021).

31. O. Devinsky, A. Vezzani, T.J. O'Brien, N. Jette, I.E. Scheffer, M. de Curtis, and P. Perucca, "Epilepsy," Nat Rev Dis Primers **4**(1), 18024 (2018).

32. N.R. Evans, J.M. Tarkin, J.R. Buscombe, H.S. Markus, J.H.F. Rudd, and E.A. Warburton, "PET imaging of the neurovascular interface in cerebrovascular disease," Nat. Rev. Neurol. **13**(11), 676–688 (2017).

33. M.D. Sweeney, S. Ayyadurai, and B.V. Zlokovic, "Pericytes of the neurovascular unit: key functions and signaling pathways," Nat. Neurosci. **19**(6), 771–783 (2016).

34. M.T. Colonnese, M.A. Phillips, M.C. Paton, K. Kaila, and A. Jasanoff, "Development of hemodynamic responses and functional connectivity in rat somatosensory cortex," Nat. Neurosci. **11**(1), 72–79 (2008).

35. F.F. Klett, N. Offenhauser, U. Dirnagl, J. Priller, and U. Lindauer, "Pericytes in capillaries are contractile in vivo, but arterioles mediate functional hyperemia in the mouse brain," Proceedings of the National Academy of Sciences **107**(51), 22290–22295 (2010).

36. S.F. Muldoon, V. Villette, T. Tressard, A. Malvache, S. Reichinnek, F. Bartolomei, and R. Cossart, "GABAergic inhibition shapes interictal dynamics in awake epileptic mice," Brain **138**(10), 2875–2890 (2015).

37. H. Matsuoka, M. Nakamura, T. Ohno, J. Shimabukuro, T. Suzuki, Y. Numachi, and S. Awata, "The role of congnitive-motor function in precipitation and inhibition of epileptic seizures," Epilepsia **46**(s1), 17–20 (2005).

38. A. Nadort, K. Kalkman, T.G. van Leeuwen, and D.J. Faber, "Quantitative blood flow velocity imaging using laser speckle flowmetry," Sci. Rep. **6**(1), 25258 (2016).

39. T. Kirchner, J. Gröhl, M.A. Herrera, T. Adler, A.H. Aguilera, E. Santos, and L.M. Hein, "Photoacoustics can image spreading depolarization deep in gyrencephalic brain," Sci. Rep. **9**(1), 8661 (2019).

40. A.A. Shemetov, M.V. Monakhov, Q.R. Zhang, J.E. Canton-Josh, M. Kumar, M.M. Chen, M.E. Matlashov, X. Li, W. Yang, L.M. Nie, D.M. Shcherbakova, Y. Kozorovitskiy, J.J. Yao, N. Ji, and V.V. Verkhusha, "A near-infrared genetically encoded calcium indicator for in vivo imaging," Nat. Biotechnol. **39**(3), 368–377 (2021).

41. Y.C. Wang, G.R. Liang, F. Liu, Q. Chen, and L. Xi, "A long-term cranial window for high-resolution photoacoustic imaging," IEEE Trans. Biomed. Eng. **68**(2), 706–711 (2021).

42. G. Kozák and A. Berényi, "Sustained efficacy of closed loop electrical stimulation for long-term treatment of absence epilepsy in rats," Sci. Rep. **7**(1), 6300 (2017).

43. K. Kotliar, C. Hauser, M. Ortner, C. Muggenthaler, J.D. Schmid, S. Angermann, A. Hapfelmeier, C. Schmaderer, and T. Grimmer, "Altered neurovascular coupling as measured by optical imaging: a biomarker for Alzheimer's disease," Sci. Rep. **7**(1), 12906 (2017).

44. C.G. Salas, B.F. Rodríguez, J.A. Pineda-Pardo, R.R. Rojas, I. Obeso, F.H. Fernández, M. del Álamo, D. Mata, P. Guida, C.O. Bandera, J.I.M. Roblas, R.M. Fernández, G. Foffani, I. Rachmilevitch, and J.A. Obeso, "Blood-brain barrier opening with focused ultrasound in Parkinson's disease dementia," Nat. Commun. **12**(1), 779 (2021).